ELSEVIER

Magnetic diphase nanostructure of $ZnFe_2O_4/\gamma$-Fe_2O_3

Xiangxi Bo[a], Guangshe Li[a], Xiaoqing Qiu[a], Yanfeng Xue[b], Liping Li[a],*

[a]*State Key Structural Chemistry Laboratory and Fujian Institute of Research on the Structure of Matter, Graduate School of Chinese Academy of Sciences, Fuzhou 350002, P.R. China*
[b]*Department of Physics, Jilin University, Changchun 130023, P.R. China*

Abstract

Magnetic diphase nanostructures of $ZnFe_2O_4/\gamma$-Fe_2O_3 were synthesized by a solvothermal method. The formation reactions were optimized by tuning the initial molar ratios of Fe/Zn. All samples were characterized by X-ray diffraction, thermogravimetric analysis, infrared spectroscopy, and Raman spectra. It is found that when the initial molar ratio of Fe/Zn is larger than 2, a diphase magnetic nanostructure of $ZnFe_2O_4/\gamma$-Fe_2O_3 was formed, in which the presence of $ZnFe_2O_4$ enhanced the thermal stability of γ-Fe_2O_3. Further increasing the initial molar ratio of Fe/Zn larger than 6 destabilized the diphase nanostructure and yielded traces of secondary phase α-Fe_2O_3. The grain surfaces of diphase nanostructure exhibited a spin-glass-like structure. At room temperature, all diphase nanostructures are superparamagnetic with saturation magnetization being increased with γ-Fe_2O_3 content.
© 2007 Elsevier Inc. All rights reserved.

Keywords: Solvothermal; $ZnFe_2O_4$; γ-Fe_2O_3; diphase nanostructure; superparamagnetic

1. Introduction

Ferrite nanocrystalline materials can be used in magnetic recording medium, information storage, bioprocessing, catalyst, and magnetooptical devices because of their promising physical properties [1–5]. Among these magnetic materials, spinel-type ferrites have gained prodigious importance. As is well known, spinel ferrite oxide can be described by a formula AB_2O_4, where A and B denote the cations that are located at tetrahedral and octahedral sites, respectively. According to the valence states of A and B cations, spinel ferrite oxides can be divided into two types of structures: normal and inverse ones to show diverse magnetic properties. Bulk $ZnFe_2O_4$ is a normal spinel ferrite in which Zn^{2+} cations at A sites are nonmagnetic and the magnetic moments of Fe^{3+} cations at B sites align anti-parallel each other. Consequently, bulk $ZnFe_2O_4$ is antiferromagnetic. However, when the particle size of $ZnFe_2O_4$ is varied within the nanoscale regime, ferrimagnetic or superparamagnetic structures appear [2–4,6],

strongly depending on the preparation methods and particle sizes. Consequently, the origin of abnormal magnetic phenomenon in $ZnFe_2O_4$ nanocrystals remains in controversy. Several research groups proposed that the magnetic properties of $ZnFe_2O_4$ are controlled by the super-exchange interactions that are introduced by modification of the distribution of Zn^{2+} and Fe^{3+} ions at A and B sites [2,3,6], while others [4,5] have concluded that nonstoichiometry or inclusion of nonmagnetic zinc ions and the resulting magnetic disorder can be the possible causes. These controversies on the magnetic properties of $ZnFe_2O_4$ nanocrystals have put uncertain impacts on the development of new ferrite functional materials.

Experimental results reported previously in literature have shown that the magnetic properties of ferrite materials are determined by phase composition and microstructure [7–9]. It has been reported that the preparation of $ZnFe_2O_4$ nanocrystals is generally accompanied by segregation of secondary phases including γ-Fe_2O_3 [10]. Unfortunately, it is still very difficult to distinguish these possible component phases from $ZnFe_2O_4$ nanocrystals because all intensive diffraction peaks for these component phases have much closer d-spacings to

*Corresponding author. Fax: +86 591 8371 9460.
E-mail address: lipingli@fjirsm.ac.cn (L. Li).

those of $ZnFe_2O_4$ due to their spinel structures in common. As a result, most of the literature work has excluded the diphase nanostructures as the causes to the total magnetism of $ZnFe_2O_4$ nanocrystals. Indeed, the structural stability of γ-Fe_2O_3 nanocrystals significantly increases with particle size reduction [11,12], and therefore γ-Fe_2O_3 nanocrystals could be one of the most likely component phases during the formation of $ZnFe_2O_4$. In addition, γ-Fe_2O_3 can be ferromagnetic or superparamagnetic at room temperature, depending on the particle sizes and preparation methods [13–16]. It is expected that γ-Fe_2O_3 would contribute to the total magnetism to some extent, if it coexisted as a diphase nanostructure with $ZnFe_2O_4$. However, experimental identification and magnetic properties of diphase nanostructures of $ZnFe_2O_4$/γ-Fe_2O_3 are still unattainable.

In this work, we studied the optimum preparation conditions to diphase nanostructures of $ZnFe_2O_4$/γ-Fe_2O_3 by altering the initial Fe/Zn molar ratios of the solvothermal reaction system. By carefully characterizing the phase compositions and structural stability features, we explored the magnetic properties of diphase nanostructures as a function of γ-Fe_2O_3 content.

2. Experimental section

$Fe(NO_3)_3 \cdot 9H_2O$ and $Zn(Ac)_2 \cdot 2H_2O$ were used as the starting materials, and NaOH was employed as the mineralizer for low-temperature crystallization. A typical preparation procedure can be described as follows: firstly, 0.01 mol $Fe(NO_3)_3 \cdot 9H_2O$ and 0.005 mol $Zn(Ac)_2 \cdot 2H_2O$ were dissolved in 30 mL ethanol while stirring. Then, 50 mL of 0.8 M NaOH solution in ethanol was added to this solution to form a brown suspension at pH = 7. After stirring for 0.5 h, this suspension was then transferred to 25 mL Teflon-lined stainless-steel autoclaves, which were allowed to react at 200 °C for 12 h. Sample A was obtained after washing with distilled water for several times and dried at 130 °C in an oven. Following this preparation procedure, samples B, C, D, and E were obtained, respectively, using initial Fe/Zn mole ratios ranging from 2 to 6.4 at the same pH value. The phase compositions of all as-prepared samples were analyzed by increasing the sample crystallinity via annealing at 700 °C for 1 h in air. The samples thus obtained were named as A700, B700, C700, D700, and E700.

The structures of the samples were characterized by X-ray diffraction (XRD) on Rigaku DMAX2500 X-ray diffractometer using a copper target. Silicon powder was used as internal standard for peak position determination. Average crystallite sizes of the samples were estimated by Scherrer formula, $D = 0.9\lambda/(\beta \cos\theta)$, where λ (= 0.15418 nm) is the X-ray wavelength, θ the diffraction angle of most intense diffraction peak (311) and (104) for $ZnFe_2O_4$ and α-Fe_2O_3, respectively.

Water content and phase transformation of the samples were determined using thermogravimetric analysis (TGA)

combined with a differential thermal analysis (DTA) on Netzsch STA449C thermogravimetric analyzer at a heating rate of 15 °C/min. The infrared spectra were recorded on a Perkin-Elmer IR spectrophotometer by using a KBr pellet technique. Raman data were collected using a JY-HR800 spectrometer with a He–Ne laser. The excitation wavelength is 632.8 nm and output powder is 20 mW. Chemical analysis of the samples was carried out using inductively coupled plasma (ICP) technique on a Perkin-Elmer Optima 3300 DV spectrometer.

BET specific surface areas of the samples are measured by N_2 adsorption isotherms at 77 K with P/P_0 equal to 0.3 on a Micromeritics ASAP 2000 surface area and porosity analyzer, where P is the pressure at equilibrium and P_0 the adsorbent vapor pressure at the measurement temperature. The magnetization curves of the samples were recorded at room temperature under an applied field of 80 KOe using a Quantum Design PPMS-7 magnetometer.

3. Results and discussion

The optimum formation conditions to diphase nanostructures of $ZnFe_2O_4$/γ-Fe_2O_3 were investigated by varying the initial mole ratios of Fe to Zn. Fig. 1a shows XRD patterns of the as-prepared samples. It is seen that samples A–D gave intensive XRD patterns responsible for spinel structures (JCPDS no. 22-102). Chemical analysis by ICP indicated that the molar ratios of Fe/Zn in samples A–E were much closer to the initial ones. From these results, it is still very difficult to determine if these samples are in a single spinel phase or a diphase nanostructure, since all intensive diffraction peaks for component ferrites $ZnFe_2O_4$ and γ-Fe_2O_3 have much closer d-spacings (see vertical bars at the bottom of Fig. 1a). When the initial molar ratio of Fe/Zn is larger than 2, all diffraction peaks became broadened, indicating the fine nature or the presence of diphase nanostructures. Further increasing the initial molar ratios of Fe to Zn larger than 6 (sample E) destabilized the spinel nanostructures to show traces of α-Fe_2O_3 (Fig. 1a), though the intensive diffraction peaks for the dominant spinel phase did not have any pronounced changes.

To confirm the phase compositions, samples with initial molar ratios of Fe/Zn < 6 were annealed in air at high temperatures for 1 h so as to increase the crystallinity. As indicated in Fig. 1b, after annealing at 700 °C, sample A with an initial molar ratio of Fe/Zn = 2 still remained in a single spinel phase. The only difference for the annealed and un-annealed sample A is in the crystallite sizes: 5 nm for the initial sample A, which compares to 35 nm for A700. By contrast, samples B700, C700, and D700 were a mixture containing α-Fe_2O_3, as shown in Fig. 1(b) for typical sample D700, which implies that the as-prepared samples B, C, and D might be in a diphase nanostructure of $ZnFe_2O_4$/γ-Fe_2O_3. The crystallite sizes of $ZnFe_2O_4$ and α-Fe_2O_3 phases in B700, C700, and D700 were calculated by XRD peak broadening. The results indicated that the
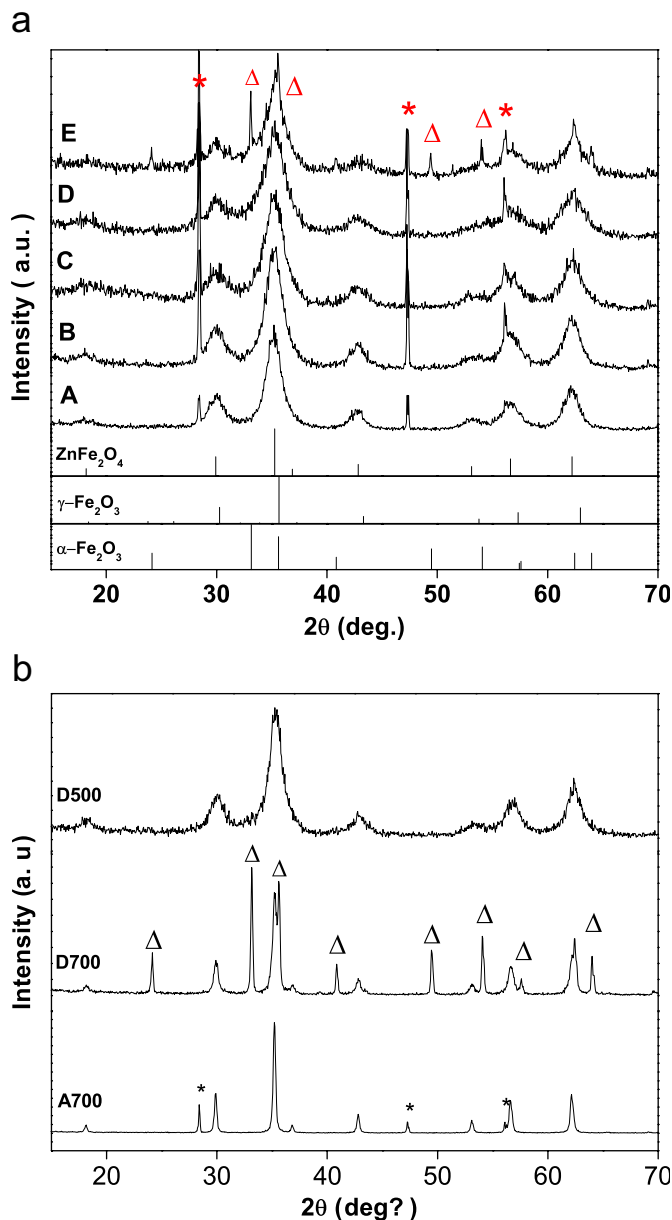
Fig. 1. XRD patterns of (a) the as-prepared samples under solvothermal methods and (b) samples A700, D700, and D500. Symbols * and Δ denote the internal standard Si and α-Fe$_2$O$_3$, respectively. Standard diffraction data for ZnFe$_2$O$_4$ (JCPDS no. 22-102), γ-Fe$_2$O$_3$ (JCPDS no. 39-1346), and α-Fe$_2$O$_3$ (JCPDS no. 33-0664) are also shown as vertical bars for comparison.
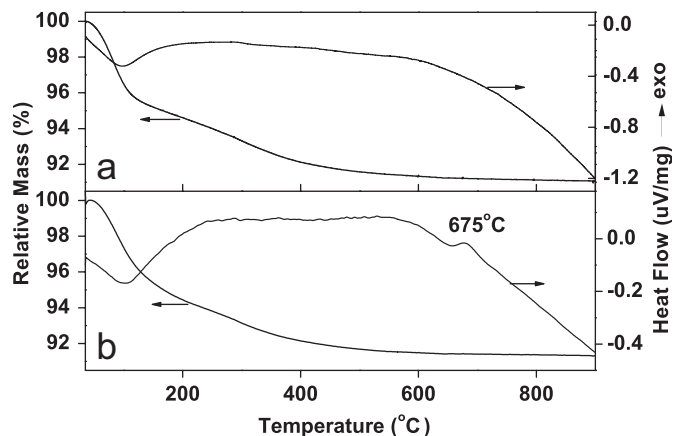

Fig. 2. TG-DTA curves of samples A (a) and D (b).

Table 1
Initial molar ratios of Fe/Zn and experimentally obtained S_{BET}, $\Delta m/m$, T_p, and D_{XRD}

Sample	A	B	C	D
Molar ratio (Fe/Zn)	2.00	2.67	4.00	5.60
$\Delta m/m$ (%)	8.9	10.1	8.7	11.3
Transition T_P (°C)		674	678	675
D_{XRD} (nm)	5.04	4.52	3.78	3.29
S_{BET} (m^2 g^{-1})	149.5	176.5	195.7	230.0
	40[a] (γ-Fe$_2$O$_3$)	78[b] (ZnFe$_2$O$_4$)		

Note: T_p is the phase transition temperature of γ-Fe$_2$O$_3$ to α-Fe$_2$O$_3$, and $\Delta m/m$ is the relative mass. Both T_p and $\Delta m/m$ were determined by thermal analysis. D_{XRD} is the crystallite sizes that were estimated from XRD peak broadening using Scherrer formula. Symbols a and b represent the literature data from Refs. [14,34], respectively.

Thermal behaviors of the as-prepared samples A and D were examined by TGA–DTA. As indicated in Fig. 2, a sharp mass loss occurred in a temperature interval from 40 to 140 °C, which corresponds to the loss of physisorbed water on surfaces [18]. The second mass loss is observed in a wide temperature interval from 140 to 600 °C, which is followed by an unnoticeable endothermic peak due to dehydration of chemisorbed water. This observation can be explained in terms of the significant surface hydration effects. When the particle size was reduced to the nanoscale regime, surface and interface components may become dominant. The broken and uncoordinated bonds would result in increased surface energies. Just like what was theoretically predicted for CaWO$_4$ [19], several hydration layers present on surfaces could decrease the surface energies and therefore can stabilize the nanostructures. Such a surface hydration might be consisted by several water molecule layers that existed at a wide set of energetically nonequivalent sites for a gradual dehydration. The total mass losses of as-prepared samples (Table 1) did not have any pronounced changes with varying the ratios of Fe to Zn, which ruled out the possibility for FeOOH in the as-prepared samples. This assumption is confirmed by

crystallite sizes for ZnFe$_2$O$_4$ phase in B700, C700, and D700 are all averaged about 20 nm, which are smaller than 35 nm for sample A700. On the other hand, the crystallite sizes of α-Fe$_2$O$_3$ in these samples remain almost the same at 50 nm. These results demonstrated that an excess of Fe in the initial molar ratio (>2) could suppress the coarsening of ZnFe$_2$O$_4$ nanocrystals and are therefore in favor of the formation of diphase nanostructures, while the intermediate wustite-type phase [17] such as those observed in ZnFe$_2$O$_4$ nanocrystals prepared by mechanosynthesis could be completely supressed.

the absence of the exothermic peak at 300 °C for decomposition of FeOOH [20]. It is also noted that Fe_3O_4 is another spinel compound. But for the present diphase nanostructures, Fe_3O_4 or oxide-phase intermediates between maghemite and magnetite is not likely a component phase, since the characteristic exothermic peak for their oxidation to γ-Fe_2O_3 [21] can be barely seen in DTA at around 160 °C (Fig. 2). When the temperature was increased higher than 600 °C, samples B, C, and D showed an exothermic peak at about 680 °C with no mass losses observed, which corresponded to a phase transformation from γ-Fe_2O_3 to α-Fe_2O_3, since XRD patterns of samples (e.g., D500) obtained after heating sample D at temperatures below 680 °C showed the presence of diphase nanostructures only, while those (e.g., D700) above 680 °C yielded plenty of α-Fe_2O_3 (Fig. 1b). Consequently, these thermal analysis results indicated the likely formation of a diphase nanostructure of $ZnFe_2O_4/\gamma$-Fe_2O_3, with surfaces that are highly hydrated when the initial molar ratios of Fe/Zn are larger than 2.

Fig. 3 shows the enlarged IR spectra of the samples in the ranges 400–1000 and 2500–4000 cm^{-1}. For all samples, a broad absorption band was observed at 3440 cm^{-1}, which is associated with the surface hydration layers [22], and is consistent with our TG–DTA analysis. Two strong absorption bands were observed at about 560 (v_1) and 420 cm^{-1} (v_2), which characterized the stretching vibrations of cations in tetrahedral and octahedral sites with oxygen [23], respectively. When the initial molar ratio of Fe/Zn is larger than 2, a shoulder band associated with γ-Fe_2O_3 [24] appeared at 630 cm^{-1} with its intensity being increased with the initial molar ratio, which confirms the presence of γ-Fe_2O_3 in the as-prepared samples.

Raman spectra for samples A and D are presented in Fig. 4. Raman spectrum for D700 is also given for comparison. In the region of 190–900 cm^{-1}, samples A and D gave similar broad Raman peaks centered at 355, 490, and 668 cm^{-1}, which are associated with F_{2g} and A_{1g}
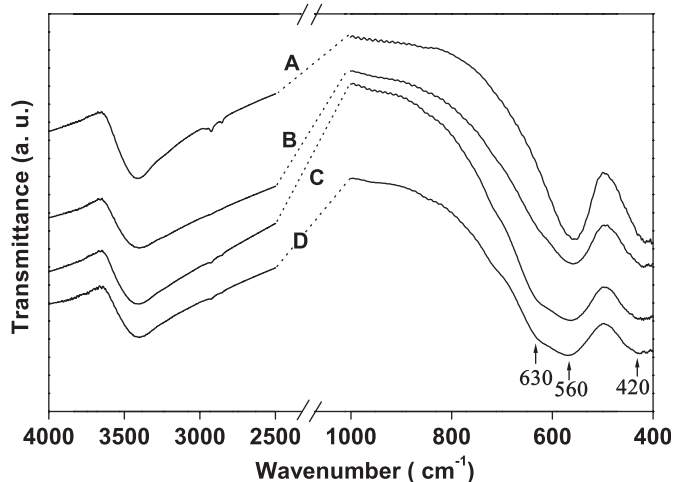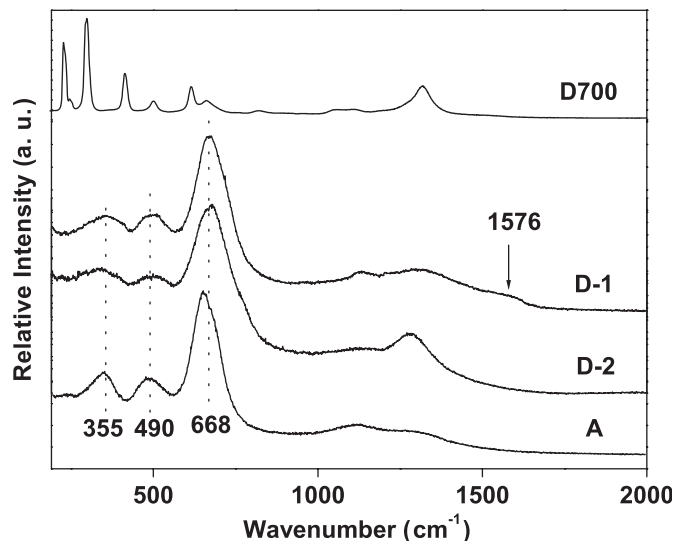

Fig. 4. Raman spectra for samples A, D, and D700. Symbols D-1 and D-2 represent the Raman spectra of sample D recorded at different spots.

modes of standard spinel structure $ZnFe_2O_4$ [25] or T_1, E, and A_1 modes of γ-Fe_2O_3 [26]. The broadened Raman modes observed for samples A and D are likely due to the diphase nanostructures and small sizes. On the other hand, for sample A with initial molar ratio of Fe/Zn = 2, XRD has indicated a pure phase of $ZnFe_2O_4$, and the Raman spectra measured at different spots are identical, which proves a homogeneous phase structure. While for initial molar ratio of Fe/Zn larger than >2, Raman spectra at different spots were different (Fig. 4). For example, Raman spectrum measured at D-2 spot showed characteristic Raman mode features of $ZnFe_2O_4$, while an additional Raman mode was observed at 1576 cm^{-1} for D-1 spot, which is associated with γ-Fe_2O_3 [27] in the diphase nanostructure $ZnFe_2O_4/\gamma$-Fe_2O_3. It is interesting that sample D700 only gave the characteristic Raman spectrum of α-Fe_2O_3, while no traces of $ZnFe_2O_4$ were observed, although XRD measurements have indicated the formation of the mixture of $ZnFe_2O_4$ and α-Fe_2O_3. To explain this observation, it is necessary to examine the formation reactions of diphase nanostructure $ZnFe_2O_4/\gamma$-Fe_2O_3.

At the beginning of the formation reaction, Zn and Fe ionic species were randomly distributed in the suspension precursor most likely in the hydrated forms of $Zn(OH)_2$ and $Fe(OH)_3$, respectively. $ZnFe_2O_4$ nanocrystals started to form when the precursor was treated at 200 °C under the adequate initial molar ratios. That is, initial molar ratio of Fe/Zn = 2 would give $ZnFe_2O_4$, while extra Fe specie for Fe/Zn > 2 led to the segregation of iron oxides in forming diphase nanostructures. With regards to the structural stabilities of α-Fe_2O_3 and γ-Fe_2O_3 nanocrystals in the diphase nanostructure, some investigations [12,28] have shown that the surface energy of α-Fe_2O_3 nanocrystals is higher than γ-Fe_2O_3. As a result, γ-Fe_2O_3 could be stabilized to several nanometers [11,29], which explains the co-existence of nanoscale γ-Fe_2O_3 with $ZnFe_2O_4$ at

Fig. 3. Enlarged IR spectra for samples A, B, C, and D in the wavenumber regions of 4000–2500 and 1000–400 cm^{-1}.

$2 < \text{Fe/Zn} < 6$. γ-Fe$_2$O$_3$ is thermodynamically metastable at ambient condition and would transform into stable α-Fe$_2$O$_3$ beyond a critical particle size. It is known that the phase transformation from γ-Fe$_2$O$_3$ to α-Fe$_2$O$_3$ could be suppressed by either ZnFe$_2$O$_4$ or size effects. Firstly, the existence of ZnFe$_2$O$_4$ in the reaction system at initial molar ratios of Fe/Zn > 2 could suppress the growth of γ-Fe$_2$O$_3$ in favor of formation of diphase nanostructure ZnFe$_2$O$_4$/γ-Fe$_2$O$_3$. However, when the initial molar ratio of Fe/Zn is larger than 6, γ-Fe$_2$O$_3$ particles would grow very fast to transform into α-Fe$_2$O$_3$. Therefore, α-Fe$_2$O$_3$ phase was detected for sample E. On the other hand, ZnFe$_2$O$_4$ also retards the phase transition from γ-Fe$_2$O$_3$ to α-Fe$_2$O$_3$ to higher temperatures. As confirmed by our TG–DTA analysis, the phase transition temperature of γ-Fe$_2$O$_3$ to α-Fe$_2$O$_3$ for our diphase nanostructures occurred at about 680 °C, which compares to that of 300 °C for bulk γ-Fe$_2$O$_3$ [30]. Secondly, size effect would be another important factor for retarding the phase transition of γ-Fe$_2$O$_3$ to α-Fe$_2$O$_3$ [11,13], (e.g., the transition temperature is 440 °C for 12 nm γ-Fe$_2$O$_3$ [31]). Zhou et al. [32], have prepared nanohybrids of nonstoichiometric zinc ferrite in amorphous silica. They found that a unique cluster glass structure occurred at the significantly high Fe/Zn molar ratio, in which zinc ferrite nanocrystals exist as amorphous Fe-rich pockets. Following this structural model, we assume that ZnFe$_2$O$_4$ particles in our diphase nanostructures are surrounded by Fe-rich pockets of γ-Fe$_2$O$_3$ which is seemly consistent with the slightly distinct Raman spectra as observed at different detected spots (e.g., D-1 and D-2 in Fig. 4). This assumption is also likely to occur since γ-Fe$_2$O$_3$ pockets over ZnFe$_2$O$_4$ nanocrystals could transform into kinetically stable α-Fe$_2$O$_3$ layers in a subsequent high-temperature treatment. We did observe only the Raman spectral features of terminal α-Fe$_2$O$_3$ layers for sample D700 (Fig. 4), although the possibility from the much larger Raman scattering power of α-Fe$_2$O$_3$ in comparison with that of ZnFe$_2$O$_4$ or γ-Fe$_2$O$_3$ could not be dismissed here [33].

Specific surface areas of diphase nanostructure ZnFe$_2$O$_4$/γ-Fe$_2$O$_3$ are given in Table 1, The literature data reported for γ-Fe$_2$O$_3$ and ZnFe$_2$O$_4$ are also given for comparison [14,34]. It is seen that at the similar particle sizes, the specific surface areas of our diphase nanostructures are much larger than 78 and 40 m^2/g reported in literature [14,34] for ZnFe$_2$O$_4$ and γ-Fe$_2$O$_3$ nanocrystals, respectively. This result indicated that our diphase nanostructures are highly dispersed. It is reasonable to conclude that the total specific surface area S_{total}, of diphase nanostructures could be described as

$$S_{\text{total}} = (1 - x)S_{\text{ZFO}} + xS_{\text{gamma}}$$
$$= S_{\text{ZFO}} + (S_{\text{gamma}} - S_{\text{ZFO}})x \qquad (1)$$

where S_{ZFO} and S_{gamma} denote the specific surface area of components ZnFe$_2$O$_4$ and γ-Fe$_2$O$_3$, respectively. The mass percentage, x, of γ-Fe$_2$O$_3$ in diphase nanostructures is

calculated when stoichiometric spinel ZnFe$_2$O$_4$ is assumed to be completely formed in the diphase nanostructures, while excess Fe ions, when subtracting the component ZnFe$_2$O$_4$ from the initial molar ratios, are all segregated as γ-Fe$_2$O$_3$. The assumption of stoichiometric components in diphase nanostructures could be reliable, as indicated by Mossbauer spectra data for all zinc ferrites and the related oxide materials that were prepared under hydrothermal conditions [2]. The total specific surface area, S_{total}, as a function of x is indicated in Fig. 5. A linear relationship is clearly seen between total specific surface area and x:

$$S_{\text{BET}} = 148.9(5) + 139(14)x,$$

where numbers 148.9(5) and 139(14) correspond to S_{ZFO} and $S_{\text{gamma}} - S_{\text{ZFO}}$, respectively, and the values in bracket represent uncertainties. This linear relationship showed that both S_{ZFO} and S_{gamma} terms are constant in diphase nanostructures. Our diphase nanostructures are an aggregate of spherical-like particles (see TEM image in inset of Fig. 5 for as-prepared sample D). It is well known that the dimensions for spherical particles can be well described as, $D = 6000/\rho S$ (where D, ρ and S denote particle size, density and specific surfaces, respectively). Therefore, the crystallite sizes for spherical particles are generally inversely proportional to the specific surface area. We anticipated that ZnFe$_2$O$_4$ and γ-Fe$_2$O$_3$ in diphase nanostructures probably have crystallite sizes being independent on the mass percentage of γ-Fe$_2$O$_3$. Using the measured specific surface areas, the crystallite sizes for ZnFe$_2$O$_4$ and γ-Fe$_2$O$_3$ in sample D were calculated to be intermediated between 4 and 8 nm, which are closer to those by TEM observations.

Magnetic properties of diphase nanostructure of ZnFe$_2$O$_4$/γ-Fe$_2$O$_3$ were examined as a function of γ-Fe$_2$O$_3$ content. Fig. 6 illustrates the room-temperature magnetization curves for samples A–D. It is seen that the
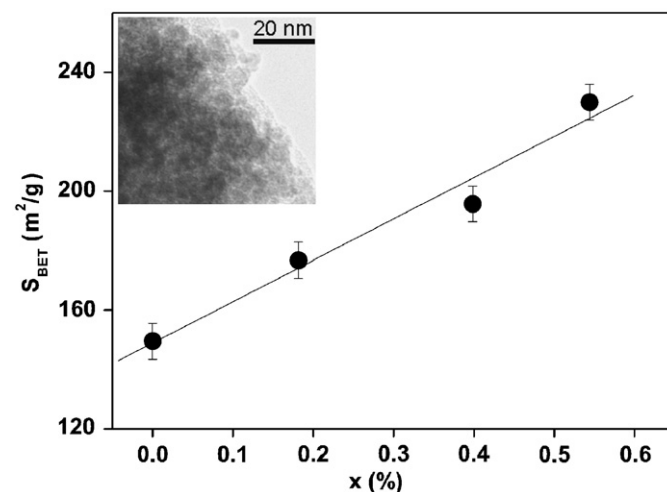

Fig. 5. Relationship of total specific surface area with mass percentage of γ-Fe$_2$O$_3$ for diphase nanostructure ZnFe$_2$O$_4$/γ-Fe$_2$O$_3$. Inset is a TEM image for the as-prepared sample D, which indicates the spherical-like shape and fine nature of the diphase nanostructures.
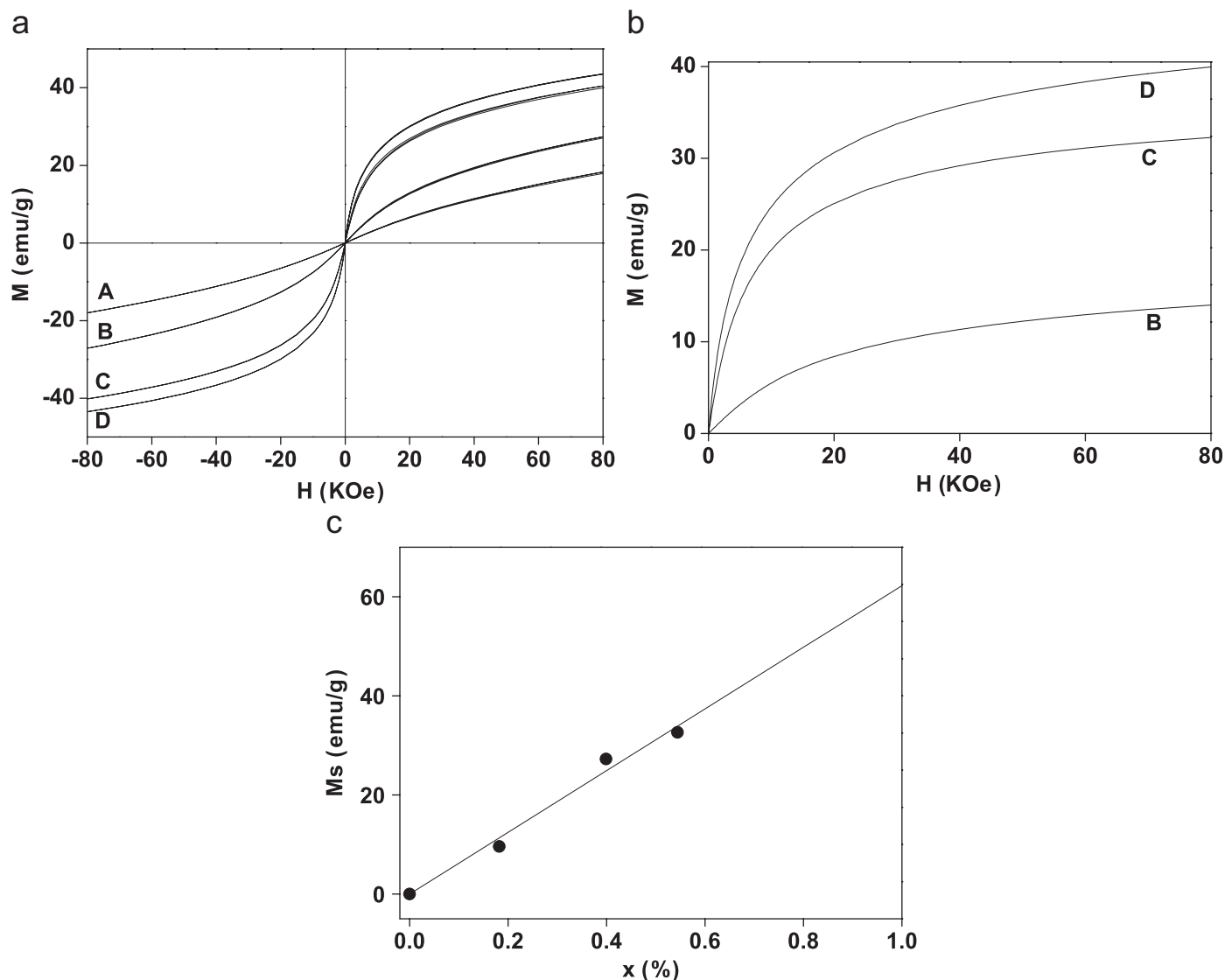
a

b

c

Fig. 6. (a) Magnetization curves for samples A, B, C and D at room temperature. (b) The initial magnetization curves obtained by subtracting the contribution of $ZnFe_2O_4$ for sample B, C, and D, and (c) the dependence of saturation magnetization, M_s, contributed by γ-Fe_2O_3 phase on the mass percentage, x, of γ-Fe_2O_3.

magnetization curves was not saturated even at a maximum external field of 80 KOe, and that the hysteresis curves for all samples are 'S' shaped with very low coercivity ($H_c \leqslant 21$ Oe), all of which are characteristic of superparamagnetism [35]. From Fig. 6a, it is also clear that the magnetization increases with the initial molar ratio of Fe/Zn. Since samples B–D exhibited a diphase nanostructure $ZnFe_2O_4$/γ-Fe_2O_3, the magnetic properties should involve the contributions from both component magnetic phases of $ZnFe_2O_4$ and γ-Fe_2O_3 and inter-particle interactions of these components as well. It is well known that surface hydration influences the magnetic behaviors of many magnetic nanoparticles by significantly reducing the inter-particle magnetic interactions [22]. The inter-particle interactions of these components were thus dismissed in this work because of the pronounced surface hydration in our diphase nanostructures (Fig. 3). Consequently, the

total magnetic properties of diphase nanostructures should be primarily correlated with the phase compositions and particle sizes. Here, the size effects could be ignored since the particle sizes for $ZnFe_2O_4$ and γ-Fe_2O_3 in these diphase nanostructures are approximately the same, as is supported by our BET measurements. Therefore, the relative content of γ-Fe_2O_3 is a dominant factor for the variations in magnetization. The total magnetization (M_{total}) of the diphase nanostructures can be descried as

$$M_{total} = (1 - x)M_{ZFO} + xM_{gamma}, \qquad (2)$$

where M_{ZFO} and M_{gama} denote the magnetization of $ZnFe_2O_4$ and γ-Fe_2O_3, respectively, while x is the mass percentage of γ-Fe_2O_3 that has already defined in Eq. (1). Here, M_{total} is a corrected value after subtracting the contribution from surface hydration effects. As stated above, the particle sizes for $ZnFe_2O_4$ were almost the same,

regardless of the initial molar ratios. Therefore, the magnetization of $ZnFe_2O_4$ can be considered constant. Bearing on this, the initial magnetization curves of γ-Fe_2O_3 in the diphase nanostructures can be obtained by subtracting the contribution of $ZnFe_2O_4$, as shown in Fig. 6(b). The saturation magnetization of γ-Fe_2O_3 can be calculated by fitting the magnetization curves using a modified Langevin function [36] in terms of the linear part observed at high fields. The relationship between the saturation magnetization from the contribution of γ-Fe_2O_3 phase and its mass percentage (x) is nearly linear, as shown in Fig. 6(c), which indicated that the magnetization of γ-Fe_2O_3 could be a fixed value in all samples. By extrapolating to $x = 1$, the saturation magnetization of 63 emu/g was obtained for γ-Fe_2O_3 component at room temperature, which is slightly smaller than that of 76 emu/g for bulk γ-Fe_2O_3 [37]. As for most of magnetic oxide nanocrystals [22,38,39], there exist plenty of uncompensated surface spins at grain boundaries and surfaces that are misaligned without any magnetic order. As a consequence, a spin-glass-like surface structure is expected in diphase nanostructures which could, however, explain the reduced total magnetism [37]. Based on the above analysis results, it can also be shown that the saturation magnetization of diphase nanostructure varied linearly with the mass percentage of γ-Fe_2O_3.

4. Conclusions

Magnetic diphase nanostructures of $ZnFe_2O_4$/γ-Fe_2O_3 were formed by varying the initial molar ratio Fe/Zn. The structural stabilities of γ-Fe_2O_3 nanocrystals in these diphase nanostructures were improved by co-existence of $ZnFe_2O_4$ nanocrystals. Diphase nanostructures showed superparamagnetic behavior at room temperature with their saturation magnetization being varied linearly with the mass percentage of γ-Fe_2O_3. The saturation magnetization of γ-Fe_2O_3 was estimated as 63 emu/g, which is much smaller than bulk γ-Fe_2O_3. These results demonstrated the existence of a spin-glass-like surface on the diphase nanostructure.

Acknowledgments

References

[1] L.P. Li, G.S. Li, R.L. Smith Jr., H. Inomata, Chem. Mater 12 (2000) 3705.

[2] J.A. Toledo-Antonio, N. Nava, M. Martinez, X. Bokhimi, Appl. Catal. A 234 (2002) 137.

[3] G.F. Goya, H.R. Rechenberg, M. Chen, W.B. Yelon, J. Appl. Phys. 87 (2000) 8005.

[4] J.F. Hochepied, P. Bonville, M.P. Pileni, J. Phys. Chem. B 104 (2000) 905.

[5] J.F. Hochepied, M.P. Pileni, J. Appl. Phys. 87 (2000) 2472.

[6] Z.H. Zhou, J.M. Xue, H.S.O. Chan, J. Wang, J. Appl. Phys. 90 (2001) 4169.

[7] A.C.F.M. Costa, E. Tortella, M.R. Morelli, R.H.G.A. Kiminami, J. Magn. Magn. Mater. 256 (2003) 174.

[8] A.M. Sankpal, S.S. Suryavanshi, S.V. Kakatkar, G.G. Tengshe, R.S. Patil, N.D. Chaudhari, S.R. Sawant, J. Magn. Magn. Mater. 186 (1998) 349.

[9] A. Verma, T.C. Goel, R.G. Mendiratta, M.I. Alam, Mater. Sci. Eng. B 60 (1999) 156.

[10] T. Kodama, J. Mater. Chem. 2 (1992) 525.

[11] P. Ayyub, M. Multani, M. Barma, V.R. Palkar, R. Vijayaraghavan, J. Phys. C. 21 (1988) 2229.

[12] G. Schimanke, M. Martin, Solid State Ion. 136–137 (2000) 1235.

[13] D.R. Chen, R.R. Xu, J. Solid State Chem. 137 (1998) 185.

[14] C. Pascal, J.L. Pascal, F. Favier, M.L. Elidrissi. Moubtassim, C. Payen, Chem. Mater. 11 (1999) 141.

[15] R.S. de. Biasi., E.C. Gondim, Solid State Commun. 138 (2006) 271.

[16] X.M. Liu, S.Y. Fu, H.M. Xiao, J. Solid State Chem. 179 (2006) 1554.

[17] T. Verdier, V. Nachbaur, M. Jean, J. Solid State Chem. 178 (2005) 3243.

[18] T. Belin, N. Guigue-Millot, T. Caillot, D. Aymes, J.C. Niepce, J. Solid State Chem. 163 (2002) 459.

[19] T.G. Cooper, N.H. de Leeuw, Surf. Sci. 531 (2003) 159.

[20] E. Moran, M.C. Blesa, M.E. Medina, J.D. Tornero, N. Menendez, U. Amador, Inorg. Chem. 41 (2002) 5961.

[21] T.J. Daou, G. Pourroy, S. Begin-Colin, J.M. Greneche, C. Ulhaq-Bouillet, P. Legare, P. Bernhardt, C. Leuvrey, G. Rogez, Chem. Mater. 18 (2006) 4399.

[22] L. Lu, L.P. Li, X.J. Wang, G.S. Li, J. Phys. Chem. B. 109 (2005) 17151 and references therein.

[23] R.D. Waldron, Phys. Rev. 99 (1955) 1727.

[24] B. Gillot, R.M. Benloucif, A. Rousset, J. Solid State Chem. 39 (1981) 329.

[25] Z.W. Wang, D. Schiferl, Y.S. Zhao, H. St. C. O'Neill, J. Phys. Chem. Solid. 64 (2003) 2517.

[26] I. Chamritski, G. Burns, J. Phys. Chem. B. 109 (2005) 4965.

[27] M.H. Sousa, F.A. Tourinho, J.C. Rubim, J. Raman Spectrosc. 31 (2000) 185.

[28] T.H. Chen, H.F. Xu, Q.Q. Xie, J. Chen, J.F. Ji, H.Y. Lu, Earth Planet. Sci. Lett. 240 (2005) 790.

[29] C. Cannas, G. Concas, D. Gatteschi, A. Musinu, G. Piccaluga, C. Sangregorio, J. Mater. Chem. 12 (2002) 3141.

[30] R.M. Cornell, U. Schwertmann, The Iron Oxides, Weinheim, VCH, 1996.

[31] X.S. Ye, D.S. Lin, Z.K. Jiao, L.D. Zhang, J. Phys. D: Appl. Phys. 31 (1998) 2739.

[32] Z.H. Zhou, J. Wang, J.M. Xue, H.S.O. Chan, J. Mater. Chem. 11 (2001) 3110.

[33] O.N. Shebanova, P Lazor, J. Solid State Chem. 174 (2003) 424.

[34] F.A. Lopez, A. Lopez-Delgado, J.L. Martin. de. Vidales, E. Vila, J. Alloy Compd. 265 (1998) 291.

[35] M.A. Khadar, V. Biju, A. Inoue, Mater. Res. Bull. 38 (2003) 1341.

[36] S.H. Kilcoyne, R. Cywinski, J. Magn. Magn. Mater. 140–144 (1995) 1466.

[37] L. Zhang, G.C. Papaefthymiou, J.Y. Ying, J. Appl. Phys. 81 (1997) 6892.

[38] A. Roy, V. Srinivas, S. Ram, J.A. De Toro, J.M. Riveiro, J. Appl. Phys. 96 (2004) 6782.

[39] L.P. Li, L.J. Chen, R.M. Qihe, G.S. Li, Appl. Phys. Lett. 89 (2006) 134102.